Autoradiographic imaging of the spatial distribution of Cl-36 in concrete

Juuso Sammaljärvi, Xiaodong Li, Stephane Gaboreau, Stéphanie Betelu, Jérôme Donnard, Paul Sardini, Marja Siitari-Kauppi, Pierre Henocq

Construction and Building Materials 456 (2024) 139279

Contents lists available at ScienceDirect

Construction and Building Materials

journal homepage: www.elsevier.com/locate/conbuildmat

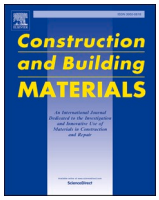

Autoradiographic imaging of the spatial distribution of Cl-36 in concrete

Juuso Sammaljärvi [a,*], Xiaodong Li [a], Stéphane Gaboreau [b], Stéphanie Betelu [b], Jérôme Donnard [c], Paul Sardini [d], Marja Siitari-Kauppi [a], Pierre Henocq [e]

[a] Department of Chemistry, University of Helsinki, A.I. Virtasen aukio 1, P.O.Box 55, Helsinki 00560, Finland
[b] BRGM, 3 avenue Claude Guillemin, BP 36009 Cedex 2, Orléans 45060, France
[c] AI4R, 2 Rue Alfred Kastler CS70727, Nantes 44300, France
[d] IC2MP, University of Poitiers, 4 rue Michel Brunet, TSA 51106 Cedex 9, Poitiers 86073, France
[e] ANDRA, 1/7 rue Jean-Monnet Cedex, Châtenay-Malabry 92298, France

ARTICLE INFO

Keywords:
Image analysis
Cl-36
Autoradiography
Concrete
Waste management

ABSTRACT

In this study, the transport properties of tritiated water (HTO) and Cl-36 in two different concretes were investigated. The spatial distribution of porosity and radionuclide retention within the studied materials were studied via C-14-Polymethylmethacrylate (C-14-PMMA) autoradiography and Cl-36 autoradiography, respectively. Diffusion experiments and modelling methods were used to calculate the effective diffusion coefficients and distribution coefficients of the tracers. The diffusivities of HTO and Cl-36 were considerably lower in mixed cement (CEMV)-based concrete than in Portland cement (CEMI)-based concrete. Autoradiography-based Cl-36 post-mortem examination revealed important distinctions explaining the diffusion behaviour between the two concrete materials. While there was considerable retention in both, in CEMV-based concrete, the diffusion was considerably slower than in CEMI-based concrete. Overall, the post-mortem autoradiographic imaging was successful, and a similar approach is probably applicable to other radionuclides.

1. Introduction

Cementitious materials are commonly used in nuclear waste management. Due to the durability of cement, it is also widely used to stabilise different hazardous waste forms [1,2]. The usefulness of cementitious materials is based on their high sorption and uptake capacity [2]. For example, in the UK concept of geological disposal of intermediate level nuclear waste (ILW) and low level waste (LLW), cementitious materials form the primary waste package intended to cause a near field reduction in the solubility of many radionuclides and retards their migration by adsorption and incorporation [3]. Cementitious materials, sometimes reinforced, are also used as a secondary barrier outside the primary waste package in more high-level waste containment and also as grouting for the confinement of the outer waste package [2]. Within the French concept of the radioactive waste deep geological repository, reinforced concrete will be used to build access structures and drifts as well as vaults and waste packages [4]. Owing to cement based materials widespread use for radionuclide immobilisation, repository construction and as secondary barriers, the behavior of radionuclides in them is required for understanding and predicting the migration of radionuclides for repository safety analyses and has therefore been the subject of numerous studies [2,5,6].

The movement of solutes in a solid cementitious matrix takes place via diffusion. Porosity influences the diffusion as diffusion takes place in the connected pore space of the concrete, with pores acting as the interface between solid and liquid phases [7]. Neutral compounds such as water, and ions other hand, might also have different effective porosity available to them [8]. The solid phase in the cementitious matrix has considerable variation, which affects its properties. The solid phase in cementitious materials is often made from composite cement where the Portland cement and one or more inorganic additives, such as fly ash (FA), blast furnace slag (BFS), silica fume (SF) and natural pozzolanas, take part in the hydration reactions [9]. Pozzolanic reactions are concurrent with cement hydration are thought to transform larger pores into smaller ones [10], leading to reduced permeability as found in water permeability tests [11] and chloride ion-mobility tests [10,11]. The liquid phase in the case of cementitious materials is the pore water solution of the cement. Solutions in equilibrium with fresh hydrated cement are hyper alkaline, with correspondingly high Na- and K concentrations. The radionuclides diffusing in a cement-based material are

* Corresponding author.
E-mail address: juuso.sammaljarvi@helsinki.fi (J. Sammaljärvi).

https://doi.org/10.1016/j.conbuildmat.2024.139279
Received 4 January 2024; Received in revised form 5 November 2024; Accepted 17 November 2024
Available online 23 November 2024

therefore in an environment containing a plethora of other, competing solutes.

Based on radionuclides' overall mobility behaviour, they can be classified into mobile, somewhat and barely mobile elements [4]. One of these mobile elements is Cl-36. Cl-36 is an important radionuclide in the low and intermediate level waste inventory (LILW) and LILW repository safety case analysis, owing to its long half-life and high mobility. Cl-36 has a half-life of 301000 ± 2000 years and it is part of the instantaneous release fraction due to its volatility [12]. It is produced from the activation of Cl-35 [13]. Due to the negative charge of chloride ions, it doesn't sorb well into most geomaterials. In clay-rich formation, however, it can experience anion exclusion, which will affect the obtained diffusion parameters [14,15] and therefore its behaviour in cementitious materials is of great interest.

In cementitious materials, chloride can experience retention through various interactions with the different phases of cement and concrete materials. The differences in the compositional makeup of the cementitious materials, such as the presence of additives, can affect the retention behaviour. The effect of different additives, such as fly ash, blast furnace slag, silica fume and metakaolin on chloride retention was studied by Thomas, et al., 2012 [16]. This study found that the greatest chloride binding was achieved with the addition of metakaolin, while the weakest binding was achieved with silica fume. The study also found that a portion of the bound chloride is released after the exposure to chloride–rich solution is stopped, but a significant portion is still bound irreversibly. A study by Ipavec, et al., 2013 [17], found that the addition of limestone hinders chloride binding as does the increased alkalinity of the pore solution. The age of the cementitious material can also influence its retention properties towards chloride as the proportion of different cement phases changes over time [18]. Several immobilization mechanisms can be behind the retention, depending on the circumstances. Some of these processes are: precipitation as a simple salt, co-precipitation with other phases, lattice incorporation in the major cement hydration products (solid solution), sorption at hydrous surfaces (chemisorption, adsorption), complex and colloid formation in the aqueous phase [5] and ion exchange. In some cases, the additives in cementitious materials can enhance the radionuclide solubility due to complex formation [19]. Chloride has several possible ways to react with cement, such as forming Friedel's salts ($C_3A*CaCl_2*10H_2O$) with unhydrated aluminate phases, forming secondary phases. Which mechanism is the dominant one, depends on the type of binder and the nature of the cations in the pore solution [5].

In the context of LILW repository constructions, studies are focused on the behaviour of Cl-36 in contact with cementitious materials used in the engineered barriers of the repository. The mobility of Cl-36 by cementitious backfill has been studied by Van Es et al., 2015 [3]. They found out that the diffusion behaviour of Cl-36 is dependent on chloride concentration and the sorption-like process takes place. The spatial distribution of the Cl-36 tracer in Nirex Reference Vault Backfill (NVRB) cement paste after a radial diffusion experiment was studied with storage phosphor screen autoradiography (SPA). Increased Cl-36 activity was found near black ash-like particles in the matrix, believed to correspond to partially hydrated glassy calcium-silicate-sulphate-rich clinker. In a study by Macé et al., 2019 [20], it was determined the spatial distribution of the Cl-36 tracer on a CEMV cement-based concrete sample using a SPA technique after a through diffusion (TD) experiment of about 12 months. Cl-36 has also been used as a tracer for environmental studies, for example to study soil carbon dynamics [21], ground water age [22] and to study the origin of perchlorate contamination) [23].

Autoradiographic imaging has been proven by these previous studies to provide in-depth knowledge of the retention process of Cl-36. Our study intends to build upon the previous knowledge base and expand it, by comparing the diffusion and retention properties of two different concrete types and incorporating new advances in autoradiographic imaging, such as the micro-pattern gas detector-based autoradiography (MPGDA), as used already successfully in geological materials [24–27], environmental samples [28,29] and for biomedical imaging [30,31]. This study, therefore, seeks to answer the following questions:

1. How do different autoradiographic techniques such as SPA and MPGDA compare to each other in imaging the spatial distribution of Cl-36 after TD experiments in cement matrices?
2. How are the differences in Cl-36 diffusion and sorption behaviour between differently prepared cementitious materials, seen in autoradiographic imaging and what can be gained from combining the results of tritiated water (HTO) and Cl-36 TD-experiments with the Cl-36 diffusion profile measured by autoradiography?

Towards these ends, the transport properties of HTO and Cl-36 in two different concretes were investigated. The spatial distribution of porosity and radionuclide retention within the studied materials were studied via C-14-polymethylmethacrylate (C-14-PMMA) autoradiography and Cl-36 autoradiography, respectively. Cl-36 autoradiography provides therefore information on the immobilized Cl-36 tracer. In addition, the effective diffusion coefficients of HTO and Cl-36 were determined via TD-experiments, providing information on the mobile phases of the tracers. A model developed based on the equation of continuity was used to interpret the experimental results and calculate the effective diffusion coefficients and distribution coefficients of the tracers.

2. Experimental

The transport properties of HTO and Cl-36 migrating through two concretes (CEMI and CEMV) were studied with TD experiments followed by post-mortem examination using SPA and MPGDA autoradiography techniques to obtain the spatial distribution of Cl-36 in the cement matrix after the diffusion of Cl-36 in the cement samples. TD experiments were performed in cylinder-shaped concrete samples to obtain the transport parameters. In addition, the samples' porosity patterns were measured by C-14-PMMA autoradiography.

2.1. Materials

2.1.1. Sample preparation

Two cement types, a CEMI 42.5 R and a CEMV/A (S-V) 42.5 N from Ciments Calcia, France, were used to prepare the concretes studied in the present work. CEMI is composed of Ordinary Portland Cement (OPC), while in CEMV part of the OPC was substituted by fly ash and blast furnace slag (Table 1). CEMI cement has a clinker content of 95 % and a maximum 5 % of other components. The clinker in CEMI has 6–11 % of C3A, 67–70 % C3S and 8–11 % C2S and 3.2–7.5 % of sulphite. CEMV has clinker content of 40–64 %, where the clinker has 7–10 % of C3A, 67–69 % of C3S, 9–11 % of C2S and sulphite content of 2.6 %. There is also 18–30 % of blast furnace slag and 16–30 % of fly ash. CEMI concrete had a hydration time of 1 month, while the CEMV concrete had a hydration of 6 months due to the slower strength development and rate

Table 1
Composition of the CEMI 42.5 R and CEMV/A (S-V) 42.5 N-based concretes.

Component	Mix proportions (kg/m^3)	
	CEMI concrete	**CEMV concrete**
CEM V/A 42.5 N	-	498
CEM I 42.5 R	498	-
Filler sibelco C6	83	83
Water	162	162
Sand 0/4 (mm)	1001	1001
Gravel 4/6 (mm)	334	334
Gravel 6/10 (mm)	331	331
SIKA tempo 9	5	5
Water-cement-ratio	0.33	0.33

of hydration of mixed cements [11]. The concretes were molded into 10 cm long cylinders with a diameter of 3.5 cm. Cylinder-shaped subsamples for TD experiments and porosity analyses were then prepared from the molded samples by sawing.

2.1.2. Radionuclide tracer solutions

In order to mimic the in situ conditions, the tracers; HTO and Cl-36, were diluted into a synthetic cement pore water solution, whose composition is shown in Table 2. All the diffusion samples were also equilibrated in the synthetic cement pore water solution for one month before the TD experiments were started.

The two radioactive tracers (mixed into the synthetic pore water solution) used in the study are shown in Table 3. Both tracers are beta emitters (H-3 E_{max}= 18 keV, Cl-36 E_{max}= 710 keV) that can be readily measured with techniques such as liquid scintillation counting and autoradiography. The half-lives of the tracers are also suitable for long-term (270 days) diffusion experiments. The Cl-36 tracer solutions were prepared by diluting a stock solution with a specific activity of 4.960 MBq±1.4 % (1.4.2017) purchased from the Czech Metrological Institute, Brno, Czech Republic. The Cl-36 was in the form of NaCl with carrier concentration being 40 g/l. The total Cl concentration in the Cl-36 tracer solution was 0.72 mM. HTO solution was prepared from a stock solution with a specific activity of 37 MBq/g (11.4.2017) purchased from Perkin Elmer.

All the experiments were conducted in a nitrogen glovebox, with the oxygen concentrations staying mostly under 10 ppm and the carbon dioxide concentration mostly less than 1 ppm. This precludes cement carbonation-related degradation during the experiment and mimics the anoxic post-closure repository conditions.

2.2. Methods

2.2.1. Porosity measurements

As the diffusion takes in place in the connected pores of cement material, it is also necessary to study the porosity of the material. Porosity is also a required parameter for the modelling used to obtain effective diffusion coefficients and distribution coefficients. Therefore, the porosity of the CEMI and CEMV concrete materials was studied by water gravimetry, Hg-porosimetry and C-14-PMMA autoradiography. ^{14}C PMMA autoradiography method involves impregnation of centimeter-scale samples with C-14-labeled methyl-methacrylate (MMA), a low molecular weight and low-viscosity monomer that infiltrates well the pore space. The labeled MMA is then polymerized with gamma radiation or heating, which results in a solid radiolabeled polymer, PMMA, within the pore network. It can provide quantitative 2D porosity mapping showing the heterogeneous connected pore network of the material [32,33]. This method is already employed for cement and clay materials [34–39].

Hg-porosimetry was performed at BRGM on parallel, 1.0–1.5 g samples. The results were handled on AutoPore IV 9500 Mercury Intrusion Porosimeter system. A pressure gradient of 0.003 MPa to 213.6 MPa was applied, which corresponds approximately to pore throat size of 7 nm. The volume of mercury penetrating the sample is a function of pressure and characteristics of the porous medium. With the assumption of cylindrical pores, the pressure can be converted into pore radius according to the Washburn equation.

Table 2
Synthetic cement pore water composition, adapted from Macè, et al., 2019 [20].

Ion	Molarity (mmol/l)
Ca	0.2
Na	80
Cl	0.1
K	170
S(6)	1
OH^-	177
pH	13.25

Table 3
Diffusion experimental setup and tracer solution parameters.

Tracer	Experiment set	Diffusion time (days)	Activity concentration (Bq/ml)	Emission energy maximum (keV)	Tracer half-life
HTO	Through-diffusion	270	5000	18	12.32 a
Cl-36	Through-diffusion	270	5000	710	3.01×10^5 a

In water gravimetry, the samples were first dried to a constant weight in a vacuum oven at 55 degrees Celsius. The water gravimetry method used was based on that found in Möri, et al., 2003 [40]. After the drying, the samples were immersed in MilliQ water and weighed once a week until a constant weight was achieved, in about three weeks. During the immersion time, the samples were kept in the nitrogen glove box and only removed for weighing. After the water gravimetry measurements, the samples were dried again to constant weight.

Thereafter the samples were immersed in a solution composed of ^{14}C-MMA with an activity concentration of 157.25 kBq/ml and 0.25 (w/w)-% of a thermal initiator, azobisisobutyronitrile (AIBN) and left to immerse for one month. The C-14 stock solution was purchased from Pharmaron UK Ltd, Cardiff, UK. The C-14 was in the form of C-14-labelled methyl methacrylate with a stock solution specific activity of 169 MBq/g. After the immersion period, the samples were polymerised by heating the samples in a heat bath at 55 °C for 16 h. The polymerised samples were then sawn, cut and polished for autoradiography. The grit used for polishing was Buehler 400(P600) aluminium oxide powder and the polishing liquid was paraffin oil. The autoradiography was done by placing the polished samples on a Fujifilm BAS TR2025 phosphor imaging plate. The exposure time was three days. The imaging plates were scanned, producing digital 16-bit autoradiographs using a Fujifilm FLA-5100 scanner. These autoradiographs were handled digitally and porosity values were calculated with the help of a C-14-activity standard series. In C-14-PMMA autoradiography the grey values of the autoradiographic image are compared with the grey values produced by different specific activity standards. By taking into account the dilution of the C-14 tracer in the sample matrix and the differing densities of the tracer resin and sample matrix, local porosity values can be calculated pixel by pixel. The resolution of autoradiographic images is limited to 20 μm by the distance the C-14 β-particles travel in various solids. However, MMA can intrude into pores of even nanometer scale [41] and therefore, porosity information can be obtained even from pores of this size. Applying this calculation over the whole area of the sample produces histograms whose mean value represents the mean porosity of the studied area. The C-14-PMMA autoradiography was performed using the Storage Phosphor Autoradiography technique, which is described in detail in Section 2.2.3. [25,33,42].

2.2.2. Through-diffusion experiment

TD experiments (Fig. 1) were done using samples with a diameter of 3.5 cm and a thickness of 1 cm and HTO and Cl-36 as tracers to determine the transport properties for the concrete materials. The experimental apparatus consisted of a concrete sample placed between two plastic chambers with volumes of around 14 ml each. In the beginning, the two chambers were filled with the synthetic cement pore water solution and left to equilibrate for one month. After the equilibration, the pore water solution was drained from the inlet side, and replaced with a solution containing HTO or Cl-36 tracers. Thereafter, once a week, the solution on the other side of the concrete sample, the outlet side, was collected and measured for the tracer activity with liquid scintillation counting. The liquid volume that was collected for sampling was replaced by a similar volume of fresh synthetic pore water simulant. The

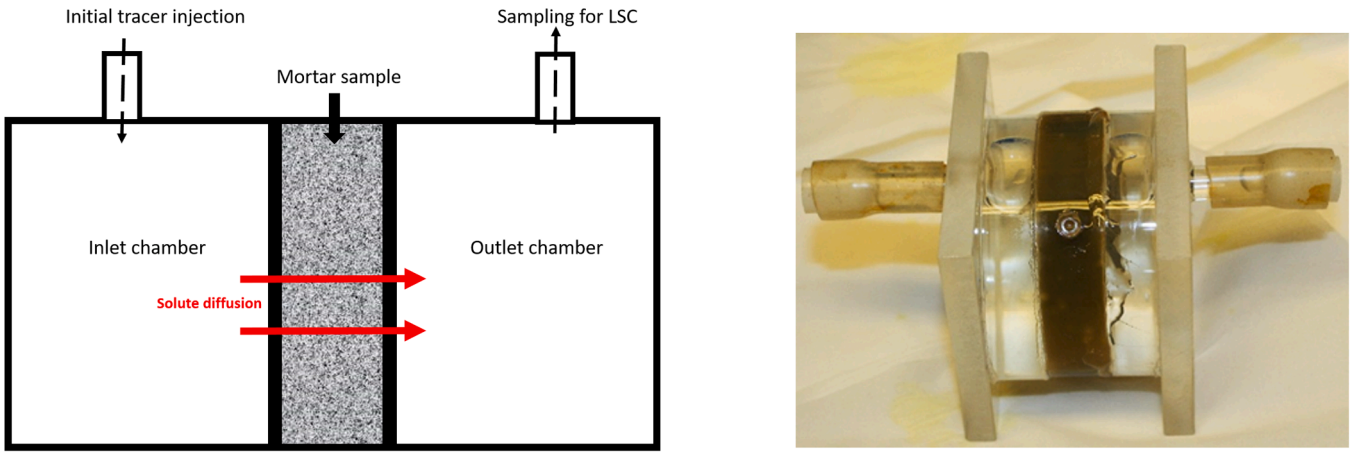

Fig. 1. Left: Schematic of the measurement setup for the TD measurements in the water phase. Edges of the samples were sealed and the ends were in contact with the high (inlet) and low (outlet) tracer concentration chambers. Right: An example of TD apparatus.

liquid scintillation counting was done with PerkinElmer Tri-Carb 2910-TR liquid scintillation counter. The samples were prepared by mixing 5 ml of sample solution and 15 ml of UltimaGold (PerkinElmer) liquid scintillation cocktail. Liquid scintillation background measurements were performed in a similar way using synthetic cement pore water without radiotracers. The counting efficiencies for Cl-36 and for HTO were determined by measuring a solution with a known Cl-36 or HTO activity in different quenched solutions (a mixture with variable water: acetone ratio as a quencher). The measurement time was 2 hours per sample. MDA for HTO was 0.2 Bq/g and 0.1 Bq/g for Cl-36.

The activities measured from the outlet chambers were plotted on a cumulative curve. The modelling approach described in 2.3 was used on these experimental results to obtain values for transport from the best fit.

After the TD experiments, the radionuclide distribution mapping was obtained by digital autoradiography on the post-mortem sawed samples as described in 2.2.3. This autoradiographic mapping shows the extent of diffusion and measures quantitatively the retention of the radionuclide tracer into different parts of the concrete. An example of the sawing scheme for samples from TD experiments is shown in Fig. 2. In this sawing scheme, a diffusion profile through the sample can be obtained from the autoradiographic imaging of cross-section surface. The Cl-36 activity found in the autoradiograph is then plotted as a function of the distance from the inlet surface as described in 2.2.3.

2.2.3. *Post-mortem analysis of the spatial distributions of Cl-36 activity by autoradiography*

Spatial distributions of Cl-36 activities on the concrete samples were measured by two measurement systems, the storage phosphor screen autoradiography with imaging plates (SPA) scanned with a Fuji FLA-5100 scanner, and the micro-pattern gas detector-based autoradiography (MPGDA) performed with the BeaQuant imaging system [43]. Both of these autoradiography techniques have complementary strengths and weaknesses [25]. SPA has good sensitivity and a wide linear range, and it is quite tolerant of artefacts caused by imperfections in the samples. SPA however doesn't allow nuclide- or radiation-specific

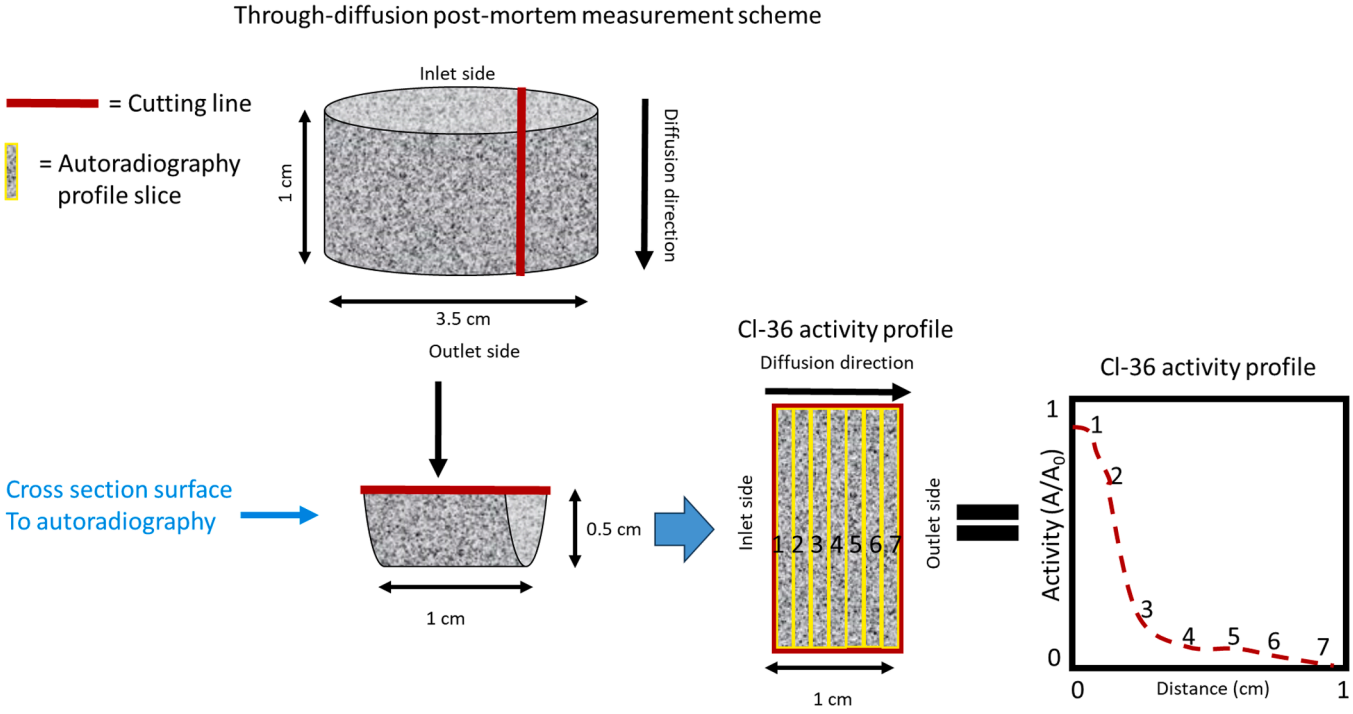

Fig. 2. TD post-mortem measurement scheme for autoradiography measurements.

imaging. The exposure times needed with SPA are also usually found via trial and error, and in any case, after about 1 week the signal fade will start to affect the results [44]. MPGDA has even better sensitivity and a wide linear range. MPGDA also allows for radiation-type, and in some cases, nuclide-specific imaging based on different radiation energies [25]. The measurement is performed straight from the sample and it detects in real-time pulses coming from the radioactive elements in the sample. There are no imaging plates or films that could be overexposed, allowing the measurement can be continued as long as necessary. The high sensitivity of MPGDA is however a disadvantage in some cases. The technique is sensitive to artefacts resulting from imperfect sample preparations and discontinuities, such as cavities [45]. Therefore, it is sensible to use two techniques of autoradiography to obtain a comprehensive characterization of the spatial distributions of activity.

In both cases, the specific activities of the studied samples were obtained with the help of standard series containing known amounts of the studied tracer nuclides, in this case, Cl-36. The standards were prepared by mixing a known amount of Cl-36 activity (65–1026 Bq/ml in prepared standards) water solution in a HEMA-MMA-monomer mixture. The resulting mixtures were then polymerized with the aid of AIBN and heated with a graduated heating program developed with Labworldsoft 3.0, with temperatures ranging from 75 to 55 °C as described in Sammaljärvi et al. [33].

Subsequently, thin discs were sawed off from the produced P(HEMA-MMA) copolymer and these discs were then polished, and the polished surfaces were coated with 10 μm of carbon to ensure good electrical conductivity across the disc. Specific activities of standard discs can be used in different autoradiographic techniques for calibrating grey levels for SPA, or cps/mm^2 for MPGDA. In SPA autoradiography, they provide a comparison between 16-bit grey scale values and specific activity, while in MPGDA they provide a comparison between cps/mm^2 and specific activity.

In SPA the calibration process starts from the conversion of grey scale values into optical densities [25]:

$$OD = \log_{10}\left(\frac{I}{I_0}\right) \tag{1}$$

Where OD is the optical density, I is the intensity of the pixel and I_0 is the mean intensity of the background. The optical density OD is related to the specific activity as described in Eq. (2)

$$OD = OD_0 \bullet A^k \tag{2}$$

Where OD_0 is the optical density of A=1 Bq/ml, A is the local specific activity, and k is the coefficient of the calibration curve. This equation can also be expressed in the following form:

$$A = \left[\frac{OD}{OD_0}\right]^{\left(\frac{1}{k}\right)} \tag{3}$$

In MPGDA, calibration is made by linearly fitting the specific activities of the standard series to the surface counting (cps/mm^2)-values obtained from the standard series.

The data obtained from the autoradiographic techniques was converted into local activities, and taking into account the beta attenuation, the local-specific activities. Spatial distributions of activity are connected phenomenon experienced by the tracer nuclides. In this case it is the diffusion and sorption into a solid matrix. The extent of the diffusion and sorption can be measured by calculation of profiles from the inlet surfaces. These profiles were obtained by calculating the local activities of thin slice-like areas of the cross-section of the sample as illustrated in Fig. 2, starting from the inlet surface towards the outlet surface. This results in the diffusion profile of the Cl-36 tracer that has retarded into the sample material and can be used in modelling the diffusion behavior of the total chloride content.

2.3. Modelling

The experimental results were interpreted with the equation of continuity describing a dilute tracer diffusing through a rock sample. According to the mass balance of a tracer ion over the studied rock sample, the concentration change of the tracer [46,47] can be written as,

$$\varepsilon_{TS}\frac{\partial c}{\partial t} = -\frac{\partial N^e}{\partial x} - \frac{\partial q}{\partial t} \tag{4}$$

where ε_{TS} is the connected porosity available for tracer ions; c is the tracer concentration in the solution of the rock sample depending on both position x and time t; N^e is the effective mass flux; and q is the tracer concentration in the solid as a result of sorption, ion exchange or chemical reactions with the solid surface.

In this model, a linear sorption isotherm is considered and Eq. (4) can be rewritten as,

$$\varepsilon_{TS}R\frac{\partial c}{\partial t} = -\frac{\partial N^e}{\partial x} \tag{5}$$

with the retardation factor R defined as,

$$R = 1 + \frac{\rho K_d}{\varepsilon_{TS}} \tag{6}$$

where ρ is the bulk density of the studied rock sample and K_d is the distribution coefficient of the tracer ions.

In Eq. (5), flux N^e can be expressed by Fick's first law in one-dimensional form,

$$N^e = -D_e\frac{\partial c}{\partial x} \tag{7}$$

where D_e is the effective diffusion coefficient. And the Eq. (6) can be rewritten as,

$$\varepsilon_{TS}R\frac{\partial c}{\partial t} = D_e\frac{\partial^2 c}{\partial x^2} \tag{8}$$

Considering the experimental processes, the following initial and boundary conditions can be applied to Eq. (8).

Initial condition,

$$c(x,0) = 0 \tag{9}$$

and boundary conditions,

$$c(0,t) = c_L(t) \tag{10}$$

$$c(L,t) = c_R(t) \tag{11}$$

where L is the length of the rock sample and c_L and c_R are the tracer concentrations in the source and recipient chambers, respectively.

With the above initial and boundary conditions, we can apply the Laplace transform to Eq. (8) and a full solution of the equation in the Laplace domain can be written as,

$$\overline{c_L} = \frac{[M_R s + S\coth(S)]M_L C_0}{[M_L s + S\coth(S)][M_R s + S\coth(S)] - S^2\operatorname{csch}(S)^2} \tag{12}$$

and

$$\overline{c_R} = \frac{S\operatorname{csch}(S)M_L C_0}{[M_L s + S\coth(S)][M_R s + S\coth(S)] - S^2\operatorname{csch}(S)^2} \tag{13}$$

where

$$S = \frac{\nu_c L}{2D_e}\sqrt{1 + \frac{4\tau_A D_e s}{\nu_c L}} \tag{14}$$

$$M_L = \frac{LV_L}{\varepsilon_{TS} RAD_e} \quad (15)$$

$$M_R = \frac{L \quad V_R}{\varepsilon_{TS} RAD_e} \quad (16)$$

and s is the Laplace variable, C_0 is the initial tracer concentration, v_c is the effective convection velocity, τ_A is the advection time, A is the cross-section area of the rock sample; V_L and V_R are the volumes of the source and recipient chambers, respectively. The numerical solution of c_R which gives the tracer concentration in the recipient chamber can be obtained by de Hoog algorithm [48] to numerically transform Eq. (13) back to the time domain. For a given experimental setup, c_R depends only on D_e, K_d and the properties of the rock sample, ε_{TS} and ρ. As a consequence, the D_e and K_d parameters can be evaluated by fitting the numerical solution c_R to the measured breakthrough curve and optimised by a least square algorithm. The modelling of the diffusion profile can be conducted by fitting the experimental data with the solutions of c_R with fixed total experimental time and varied rock sample lengths.

3. Results & discussion

3.1. CEMI concrete results

3.1.1. Results of porosity studies (CEMI)

Porosity was measured with water gravimetry and Hg-porosimetry to obtain total porosity values, and with autoradiography to obtain both total porosity values and spatial distributions of porosity. The surface scans, C-14-PMMA autoradiographs and porosity maps of the CEMI concrete sample are shown in Fig. 3. Both of the autoradiographs show that impregnation with C-14-MMA was successful and the saturation time of 1 month with C-14-MMA was sufficient. There is no spatial gradient visible in the autoradiograph that would indicate imperfect impregnation. The heterogeneity in the spatial distribution of porosity is clearly visible. While most of the rock aggregate has low porosity, there are a few porous minerals in the rock aggregate. There also appear to be a small amount of bubbles seen as black spots in autoradiographs (Fig. 3 red spots in the porosity map). Slightly higher porosities were found adjacent to the edges of the cement cylinder core indicating slight drilling disturbance.

The total porosity value obtained via water gravimetry was 14.6 ±3.5 % and 10.4±1.1 % by Hg-porosimetry, while the total porosity obtained via C-14-PMMA autoradiography was 14.7.6±1.5 %. Hg-porosimetry also gave a mean pore diameter value of 13.8 nm. C-14-PMMA autoradiography was also used to calculate the matrix porosity by excluding the macropores and the coarse rock aggregate. The cement matrix porosity obtained was determined to be 18.9±1.9 %. This result is less than the range of ordinary porosity values for cement paste [34, 39] as the concrete recipe includes a considerable amount of fine-grained sand. Most of the connected porosity is known to be found in the cement matrix. These porosity results were taken in as input parameters in the modelling.

The porosity values obtained by the used different techniques are quite close to each other. The immersion time of 32 days in water gravimetry and C-14-PMMA impregnation appears to have been sufficient to obtain full saturation of the pore space. Hg-porosimetry however gave a bit lower value. It is possible that not all of the porosity was accessible to Hg with the applied pressure. The pore apertures of intragranular porosity in the cement matrix are on a nanometer scale and tracer intrusion into the nanometer scale takes time. Sample heterogeneity is also one possible explanation for the slight differences in total porosity, as the autoradiographic measurements are from a sawn surface, while water gravimetry data is derived from the whole sample but in our experience, this problem usually cause underestimation of the porosity [38].

3.1.2. Results of through diffusion experiments (CEMI)

The through diffusion results of HTO and Cl-36 in CEMI concrete and the modelled curves are shown in Fig. 4. HTO starts to break through in about one week, while the Cl-36 breakthrough started after about 50 days of diffusion time. The considerable delay between the breakthroughs of Cl-36 compared to HTO suggests that there is an interaction between the Cl-36 tracer and the sample material.

The porosities obtained from Section 3.1.1 via C-14-PMMA autoradiography were used as input parameters in the modelling processes and, more specifically, the diffusion was modelled by using the C-14-PMMA porosity of the cement matrix (18.9±1.9 %). For the modelling with HTO data, it was assumed that HTO was an inert tracer and only diffusion controls the transport of HTO. Thus, the effective diffusion coefficient (D_e) for HTO was the only controlling parameter during the modelling process of HTO TD data. By fitting the modelled curve against experimental data, the best-fit D_e for HTO was obtained to be 6.6 $\pm 1.3\times10^{-12}$ m^2/s.

For the modelling with Cl-36 data, it was assumed that both diffusion and retardation processes will play an important role in the transport of Cl-36 in cement-based materials. Thus, both D_e and distribution coefficient (K_d) should be used as input parameters in the Cl-36 modelling. Previous studies show that a ratio of 1.3 exists in the D_e values for HTO/Cl-36 when transporting through free water [49,50] and also in the confined space of C-S-H paste which is the main phase of cement [51]. It has also been shown that in general if the diffusion coefficient of one species is known and the tortuosity of the material remain unchanged, the diffusion coefficients of other species can be calculated as well (Samson, et al., 2003) [52].

The D_e value for Cl-36 from HTO data was therefore estimated to be

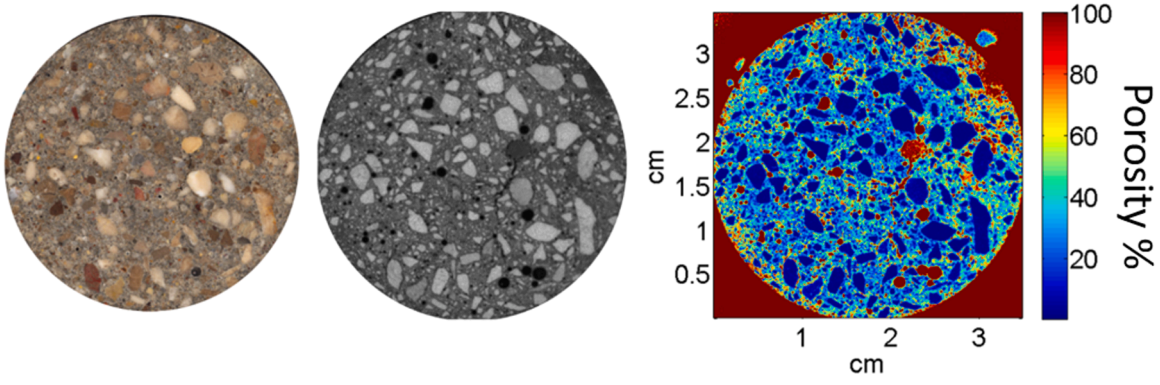

Fig. 3. Left: Surface scan of CEMI concrete sample. Centre: Corresponding C-14-PMMA autoradiograph of CEMI concrete sample. Right: Corresponding porosity map of CEMI concrete samples.

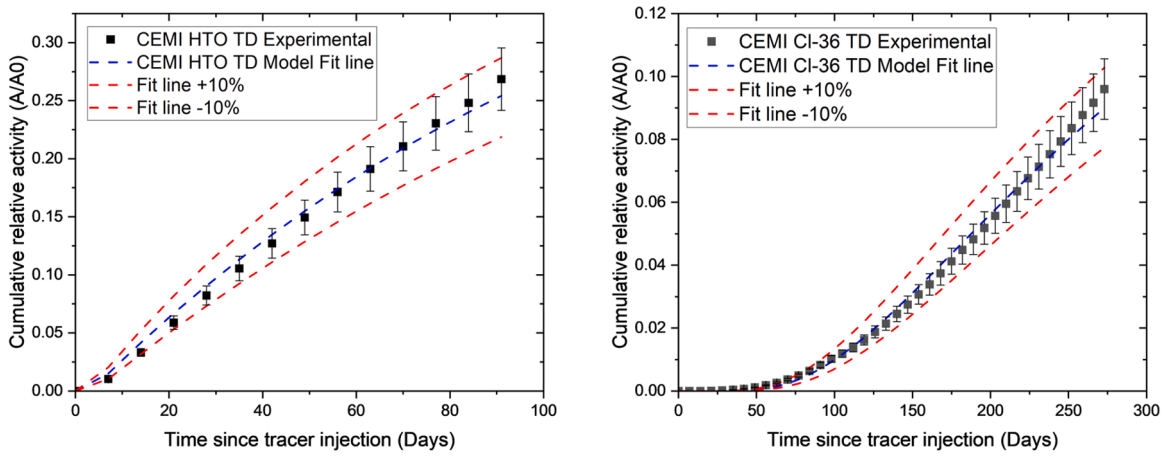

Fig. 4. Left: Through diffusion results of HTO in CEMI concrete. Right: Through diffusion results of Cl-36 in CEMI concrete. Experimental results as black dots, and modelled results as red dots.

$5.1\pm1.0\times10^{-12}$ m^2/s and this value was used as an input parameter during the modelling of Cl-36 data from autoradiography. The K_d value was the controlling parameter in the modelling procedure at this step and fitting be made solely to resolve the K_d. The best fit gives the K_d value of $1.9\pm0.2*10^{-3}$ m^3/kg. Two parameter fitting was also performed to validate the used modelling approach. With two parameters fitting, the D_e was estimated to be $5.2\pm1.0\times10^{-12}$ m^2/s and K_d was estimated to be $1.9\pm0.2*10^{-3}$ m^3/kg. This close result shows that the 1.3 ratio estimate for HTO/ Cl-36 diffusion coefficients is a valid assumption.

Post-mortem examination of the CEMI concrete was performed after the TD experiment was terminated. Four slices were cut from the CEMI concrete sample, the autoradiographs were taken and the results were averaged to account for material heterogeneity. An example of the post-mortem Cl-36 autoradiographs is shown in Fig. 5. The samples were imaged using both MPGDA- and SPA-technique based Cl-36 autoradiography and diffusion profiles of specific activity by distance from the inlet surface were calculated. The resulting activity profile is shown in Fig. 5 along with a representative example of the autoradiographic images and the corresponding sample surface. Fig. 5 clearly shows that Cl-36 diffused throughout the CEMI concrete sample while experiencing considerable retention into the cement matrix. The retention is wholly concentrated in the cement matrix; there is no notable retention in the rock aggregate. Fig. 5 shows that there is a decreasing tendency in the spatial activity in the diffusion profile towards the outlet side. This indicates that while a breakthrough was obtained, a steady state was not yet reached during the experimental time. There was also an apparent drop in the spatial activity near the inlet side surface. This is probably an artefact due to non-ideal contact between the sample and the autoradiographic imaging surface, as also reported by Macè, et al., 2019 [20]. This was taken into account by applying an offset of 1.5 mm to the activity profiles. The activity profiles obtained by MPGDA and SPA autoradiography techniques are fairly similar to each other although some differences can be discerned. The MPGDA autoradiograph appears to be slightly sharper than the SPA autoradiograph. On the other hand discontinuities, such as cavities, appears as bright spots in the MPGDA image, while such artefacts are not prominent in the SPA image.

3.2. *CEMV concrete results*

3.2.1. *Results of porosity studies (CEMV)*

Similarly as in studies with CEMI, total porosity values were obtained via water gravimetry and C-14-PMMA autoradiography, with the latter providing also the spatial distribution of porosity. The surface scans, C-

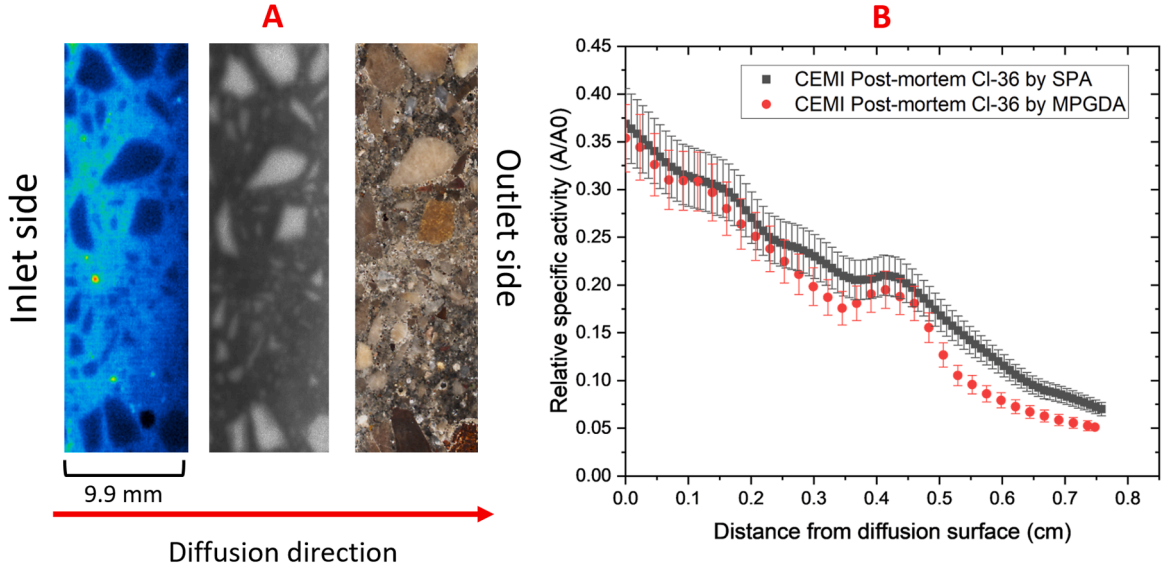

Fig. 5. A: Cl-36 autoradiography from the inlet surface in CEMI concrete by MPGDA (left) and SPA (centre) Cl-36 autoradiography and the corresponding sample surface(right). B: Spatial distribution of activity from inlet diffusion surface towards the outlet chamber as measured from autoradiographs.

14-PMMA autoradiographs and porosity maps of the CEMV concrete sample are shown in Fig. 6. Autoradiography results show that impregnation with C-14-MMA was successful. There is no spatial gradient visible in the autoradiograph that would indicate imperfect impregnation. The spatial distribution of porosity is broadly similar to that of the CEMI concrete shown in Fig. 3. The heterogeneity in the spatial distribution of porosity is apparent with the lowest porosities found in the rock aggregate and highest porosities in bubble cavities, while most of the sample area is a porous cement matrix.

The total porosity value obtained via water gravimetry was 16.4 ±2.7 %, 8.8±0.9 % by Hg-porosimetry and the total porosity obtained via C-14-PMMA autoradiography was 13.3±1.4 %. Hg-porosimetry was also to determine a median pore diameter 22.6 nm. The difference in bulk porosity value by Hg-porosimetry compared to other two methods could be due to sample heterogeneity or it is possible that not all of the porosity was accessible to Hg with the applied pressure. C-14-PMMA autoradiography was also used to calculate the matrix porosity by excluding the macropores and the rock aggregate. The matrix porosity obtained was determined to be 16.3±1.7 %. This result is in the same range as the porosity of the CEMI concrete. The pozzolanic reaction caused by pozzolanic agents, fly ash and blast furnace slag, present in CEMV, tends to cause the transformation of larger pores to smaller ones concurrent with cement hydration [10], leading especially to a reduction in the number of micrometre scale pores [53]. This however doesn't apparently cause a major reduction of overall porosity, as seen in our results. It could however affect the diffusion behaviour of the sample material because the tortuosity and the constrictivity of the pores increase. This effect could especially be seen in chloride diffusion, as pozzolanic agents are known to cause a reduction in chloride ion mobility [10] and bind chloride ions to different degrees [16].

3.2.2. *Results of through diffusion experiments (CEMV)*

The through diffusion results of HTO and Cl-36 in CEMV are shown in Fig. 7 alongside the corresponding modelled curves for HTO. HTO starts to break through after 50 days, while Cl-36 is negligible even after 270 days of diffusion time and therefore no modelling could be performed on Cl-36 TD. The results show that the diffusion of both HTO and Cl-36 in CEMV concrete was considerably slower than those in CEMI concrete. The overall decrease in diffusivity is caused by the shift in pore sizes towards nanometer scale pores caused by pozzolanic reactions. Compared to CEMI concrete the breakthrough of HTO starts about 43 days later and Cl-36 is not measured at all. This indicates that there is considerable retention of Cl-36 in the CEMV concrete.

The modelling method of the diffusion of HTO within CEMV was the same as the modelling method applied to HTO diffusion in CEMI. The same assumption that HTO was an inert tracer was also applied with CEMV, and thus diffusion was the only process that can determine HTO transport in CEMV. By finding the best fit of the modelled curve with the experimental data, the D_e value of HTO diffusion in CEMV was calculated to be $4.4\pm0.5\times10^{-13}$ m^2/s. However, because the breakthrough of Cl-36 could not be properly determined, the modelling of Cl-36 diffusivity was performed based on the HTO diffusion data and with the Cl-36 diffusion profile data.

Post-mortem examination of the CEMV concrete was performed after the through diffusion experiment was terminated. Four slices were cut and autoradiographed from the CEMV concrete sample and the results were averaged to account for material heterogeneity. The samples were imaged using both MPGDA- and SPA-technique based Cl-36 autoradiography and profiles of specific activity by distance from the inlet surface were calculated and normalized to account for the non-bound portion of the Cl-36 tracer. Modelling fit was then applied to the experimental results. The resulting activity profiles are shown in Fig. 8 along with a representative example of the autoradiographic images and the corresponding sample surface. The CEMV concrete sample imaging shows that the Cl-36 tracer had not diffused through the sample within the experimental time, which corroborates the finding that the breakthrough of chloride was not observed during 270 days of the experiment. The activity profiles presented in Fig. 8 show that the diffusion front was found at a depth of about 4–5 mm into the sample, out of the total cross-section length of 1 cm. Therefore the diffusion front had only reached about halfway into the sample, unlike in CEMI-based concrete where the Cl-36 tracer was found throughout the length of the sample. Heterogeneity in the diffusion front can be observed in CEMV concrete samples. It appears that the diffusion front is slightly more advanced around large aggregates, probably because there is negligible retention to the aggregate, allowing for faster diffusion and/or in the interface of aggregate/cement paste there is an opened grain boundaries allowing faster migration to take place. In CEMV concrete too, the retention is wholly concentrated in the cement matrix; there is no notable retention in the rock aggregate. The MPGDA and SPA-derived activity profiles are fairly similar although the MPGDA profile descends later and less sharply. Perhaps this is due to the greater sensitivity of the MPGDA technique. Another cause for the difference in the curves could be that incontinuities, such as bubble cavities, tend to appear as bright artefacts in MPGDA imaging. The same modelling method as used for CEMI concrete though-diffusion results can be adapted to be used for modelling the Cl-36 activity/diffusion profiles by examining the concentration distributions along the sample length at the last experimental time (270 days in this work). The same assumptions as applied in CEMI studies were used to estimate the D_e of Cl-36 in CEMV as $3.4\pm0.4\times10^{-13}$ m^2/s by applying a conversion factor to the D_e value of HTO [51]. Thus, K_d is the only controlling parameter in the modelling process. By best-fitting, the modelled curve to the experimental data, the K_d value of Cl-36, indicating the interaction with the CEMV material, was calculated to

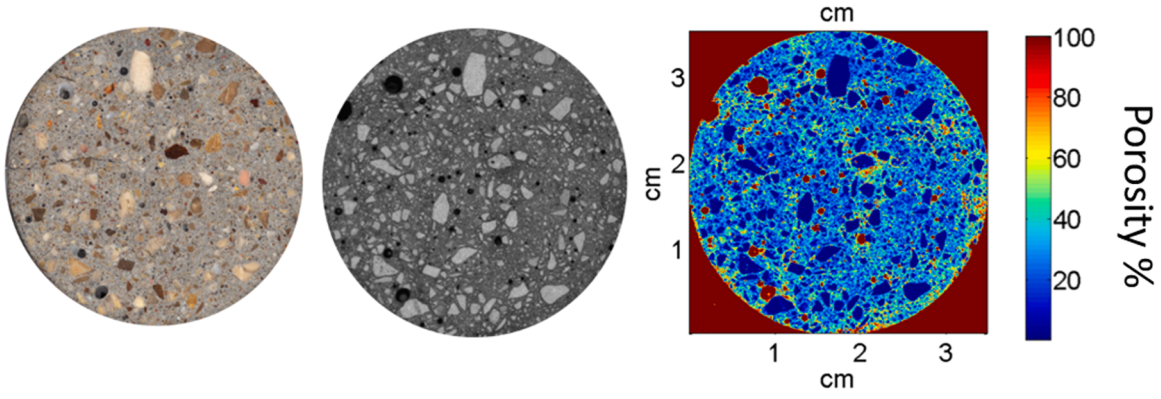

Fig. 6. Left: Surface scan of sample CEMV. Centre: Corresponding C-14-PMMA autoradiograph of sample CEMV. Right: Corresponding porosity map of sample CEMV.

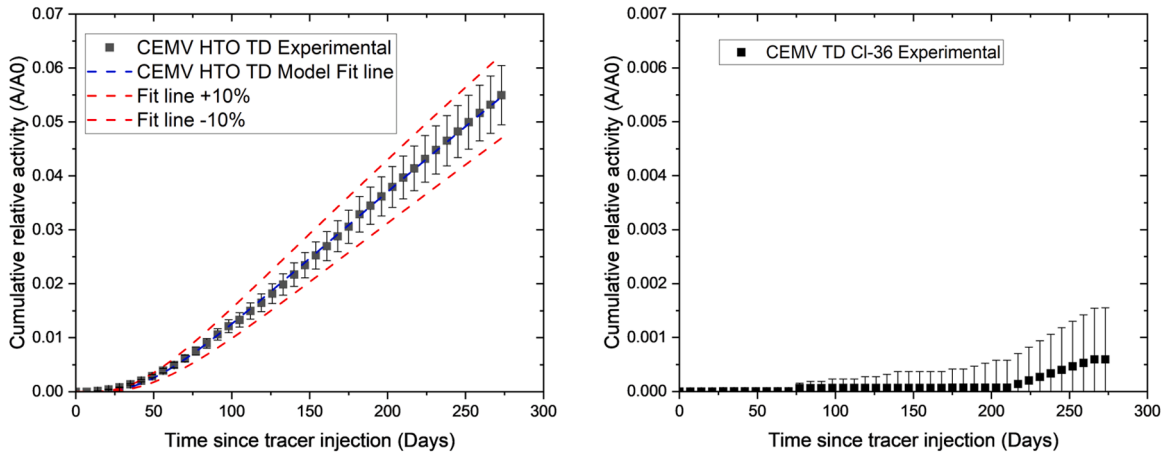

Fig. 7. Left: Though diffusion results of HTO in CEMV concrete. Experimental results as black dots, and red curve represent the modelled curve based on the experimental results. Right: Through diffusion results of Cl-36 in CEMV concrete.

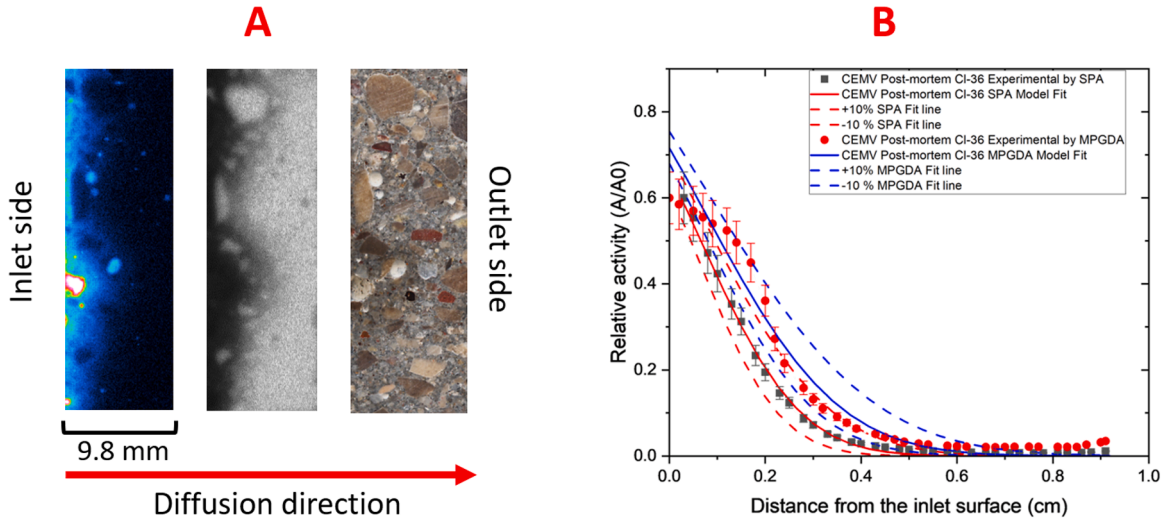

Fig. 8. A: MPGDA Cl-36 autoradiographs (left), corresponding SPA Cl-36 autoradiographs (centre) and corresponding surface scans (right) of the CEMV concrete Cl-36 samples. B: Diffusion profiles of Cl-36 in post-mortem CEMV concrete samples by SPA and MPGDA methods.

be $1.9\pm0.7\times10^{-3}$ m^3/kg. On the autoradiograph, we detect the retarded part of diffused chloride but combined this data with the diffusivities of the non-retarded tracers we can determine the total diffusivity of chloride in the samples.

The porosity values and diffusivities are presented in Table 4. The porosity values obtained for the two concretes are of the same order of magnitude and differ only slightly, even though the average pore size might be different as pozzolanic components in CEMV because of the transformation of large aperture pores to smaller aperture pores [10] via reaction with the calcium hydroxide and alkalis released during OPC hydration [11]. The pore size range in cement is however in the range of a few tens of nanometres and downwards, making it difficult to image the individual porous structure, although STED nanoscopy, as used for geological samples [54] could be used for this purpose after proper method development. It is however noted that the curing time was different in the sample types due to the differing hydration rates. The curing also affects to the diffusivity, with a general trend of decrease with increasing curing time [55,56]. This is parameter that should be controlled for too in future experiments.

Table 4
Summary of the porosity and diffusion parameters for CEMI and CEMV concrete.

Porosity parameters	CEMI concrete	CEMV concrete
Total porosity by water gravimetry	14.6±3.5 %	16.4±2.7 %
Total porosity by Hg-porosimetry	10.4±1.1 %	8.8±0.9 %
Total porosity by C−14-PMMA autoradiography	14.7±1.5 %	13.3±1.4 %
Diffusion and distribution coefficients		
Effective diffusion coefficient (HTO)	$6.6\pm1.3\times10^{-12}$ m^2/s	$4.4\pm0.5\times10^{-13}$ m^2/s
Effective diffusion coefficient (Cl−36)	$(5.2–5.1)\pm1.0\times10^{-12}$ m^2/s	$3.4\pm0.4\times10^{-13}$ m^2/s
Distribution coefficient (Cl−36)	$1.9\pm0.2\times10^{-3}$ m^3/kg	$1.9\pm0.7\times10^{-3}$ m^3/kg

There is a clear trend in all of the HTO and Cl-36 diffusion results; diffusion through CEMV is considerably slower compared to diffusion through CEMI. Total porosity values are however rather similar, suggesting that the reason for slower diffusion lies in the microstructure of the connected pore network. HTO diffusion results were consistent with the behavior of an inert tracer, but the Cl-36 diffusion showed that it experienced retention. The retention combined with slower diffusion meant that no breakthrough of the Cl-36 tracer occurred in the CEMV concrete during 270 days of the through diffusion experiment. The diffusion coefficients obtained in our experiments were in agreement with those obtained previously in other works. For example, Uusheimo, et al., 1993 [57], obtained an effective diffusion coefficient of

6.0–7.1×10^{-12} m^2/s for HTO and 4.1×10^{-12} m^2/s for Cl-36 in ordinary concrete. Macé, et al., 2019 [20], reported diffusion coefficients of 3.10×10^{-13} m^2/s for HTO and 1*10^{-13}-7.1×10^{-14} m^2/s for chloride in their CEMV concrete.

There was considerable retention of Cl-36 in both materials CEMI and CEMV. No retention of HTO could be measured using our methods and the results could be modelled well with the assumption of HTO as an inert tracer. Distribution coefficients of Cl-36 were quite close to each other suggesting similar retention potential in these concretes for chloride in our experimental conditions. Differing results have also been obtained. Thomas, et al., 2012 [16], and Ipavec, et, al, 2013 [17], reported increased chloride binding as a function of increased alumina in the supplementary cementitious materials. These studies however used considerably higher chloride concentrations, ranging from 50 mM to 3000 mM. The samples were also broken into small pieces while in our study, the samples remained intact. It is therefore possible that similar equilibrium conditions were not obtained in our study, especially in the CEMV concrete with lower permeability. Macé, et al., 2019 [20], obtained distribution coefficients of 0.0004 and 0.0005 m^3/kg for their CEMV-based concrete. This is less than obtained in our experiment. This is likely due to the lower total concentration of Cl used in our work (0.72 mM) compared to those used by Macè, et al., 2019 (30 mM) [20]. Chloride has been known to form Friedel's salt and Kuzel's salt in cementitious media, especially in higher chloride concentrations [16, 20]. Van Es, et al., 2015 [5], also found that increased Cl-36 activity in cementitious backfill was associated with black ash-like particles in the matrix, which they believed to correspond with partially hydrated glassy calcium-silicate-sulphate rich clinker. However, such a pattern of increased activity was not present in the samples of this study, perhaps owing to different concrete compositions. Our post-mortem autoradiography results showed uniform retention in the cementitious matrix. The coarse rock aggregate exhibited no retention in these results, which is consistent with the findings of Cl-36 behaviour in a crystalline rock where no retardation of Cl-36. The results were similar to those shown by Mace, et al., 2019 [20], where a similar distribution pattern was observed. The diffusion front appeared sometimes more advanced around the rock aggregates, perhaps due to different migration pathways of the interfacial transition zone (ITZ) around the rock aggregate [58]. As chloride has a considerably smaller effective diffusion coefficient in CEMV concrete than in CEMI concrete, a given volume of CEMV concrete will inhibit the movement of chlorine far longer than a similar volume of CEMI concrete.

4. Conclusions

TD experiments in two concrete samples were performed with HTO and Cl-36 tracers. The diffusivities of HTO and Cl-36 were considerably lower in CEMV concrete than in CEMI concrete. Autoradiography-based Cl-36 post-mortem examination revealed important distinctions explaining the diffusion behaviour between the two concrete materials. While there was considerable retention in both, in CEMV, the diffusion was considerably slower than in CEMI. The Cl-36 diffusion front in CEMV reached 4–5 mm into the 1 cm thick sample after 270 days of experimental time whereas it reached the other side of the 1 cm long sample in CEMI. This difference could not be explained simply with different bulk porosity values, as the bulk porosity in the two sample types was found to be roughly the same. The divergence is better explained by differences in the pore structure. CEMV-type sample had a longer hydration time and the mixed cement material, contributing to tendency to have a higher proportion of nanometer-scale pores resulting in increased tortuosity and increased constrictivity, which decreases diffusivity as well.

In the post-mortem imaging, Cl-36 diffusion profiles produced by the MPGDA seemed to have overall better resolution, but incontinuities such as bubbles in cement can cause artefacts, which appear as bright spots. The bubbles can be excluded from the diffusion profile analyses comparing the autoradiograph to the sample surface scan. Due to the artefacts, it is also reasonable to use two types of autoradiography. These kinds of artefacts could possibly also be eliminated by impregnating the samples post-mortem in suitable resin, such as MMA, followed by subsequent polymerization. Overall, the post-mortem autoradiographic imaging was successful, and a similar approach is probably applicable to other radionuclides. Possible further candidates for similar imaging could be the other mobile radionuclides of interest such as ^{129}I, ^{14}C, ^{41}Ca and ^{79}Se.

These results could be taken into account for example in choosing the cementitious material and the reaction conditions to be used in a repository containing a lot of Cl-36-waste like in low and intermediate waste cases or choosing the concrete type to be used in a waste immobilization with concrete The efficiency of a given waste immobilization material could also be measured with autoradiographic imaging. This imaging could also show if there are sites of preferential retention in the waste form for different nuclides, especially if it is possible to distinguish different nuclides in imaging, as with MPGDA. Another potential application of the imaging techniques used in this work, is the study of the degradation of cementitious materials by chloride-containing solutions, such as seawater. Concrete structures often contain other structural elements, such as steel reinforcement, which can experience corrosion due to reactions with chloride ions and autoradiographic imaging could increase the understanding of this process.

Possible future studies could be further modelling to describe the retention process and the elucidation of the role of different phases formed during the retention of chloride. This could be accomplished by complementing diffusion experiments with sorption studies into model materials representing cement paste and singular cement phases. These studies could also include nanoscopy techniques such as Stimulated Emission Depletion (STED) nanoscopy to image nanoscale porous features. A follow-up study focusing on leaching immobilized Cl-36 could be performed to account for changing conditions in a repository system. Such changing conditions can come about due to long-time-scale climate changes, such as ice ages, resulting in changes in groundwater composition.

CRediT authorship contribution statement

Xiaodong Li: Writing – original draft, Visualization, Validation, Software, Methodology, Formal analysis, Data curation. **Juuso Sammaljärvi:** Writing – review & editing, Writing – original draft, Visualization, Validation, Supervision, Software, Resources, Project administration, Methodology, Investigation, Funding acquisition, Formal analysis, Data curation, Conceptualization. **Paul Sardini:** Writing – review & editing, Writing – original draft, Methodology. **Jérôme Donnard:** Writing – original draft, Validation, Resources, Methodology. **Stéphanie Betelu:** Validation, Methodology, Investigation, Conceptualization. **Stéphane Gaboreau:** Supervision, Resources, Project administration, Methodology, Funding acquisition, Conceptualization. **Pierre Henocq:** Writing – review & editing, Writing – original draft, Validation, Supervision, Methodology, Funding acquisition, Conceptualization. **Marja Siitari-Kauppi:** Writing – review & editing, Writing – original draft, Supervision, Project administration, Methodology, Investigation, Funding acquisition, Formal analysis, Conceptualization.

Declaration of Competing Interest

The authors declare that they have no known competing financial interests or personal relationships that could have appeared to influence the work reported in this paper

Data availability

Data will be made available on request.

References

[1] R. Malviya, R. Chaudhary, Factors affecting hazardous waste solidification/stabilization: a review, J. Haz. Mat. B137 (2006) 267–276, https://doi.org/10.1016/j.jhazmat.2006.01.065.

[2] J. Kotatkova, J. Zatloukal, P. Reiterman, K. Kolar, Concrete and cement composites used for radioactive waste deposition, J. Env. Rad. 178-179 (2017) 147–155, https://doi.org/10.1016/j.jenvrad.2017.08.012.

[3] E. Van Es, J. Hinchliff, M. Felipe-Sotelo, A.E. Milodowski, L.P. Field, N.D.M. Evans, D. Read, Retention of chlorine-36 by a cementitious backfill, Min. Mag. 79 (6) (2015) 1297–1305, https://doi.org/10.1180/minmag.2015.079.6.05.

[4] ANDRA. 2005. Argile – Synthesis- Evaluation of the Feasibility of A Geological Repository in an Argillaceous Formation – Meuse/Haute-Marne site. Dossier 2005 Andra Report Series.

[5] N.D.M. Evans, Binding mechanisms of radionuclides to cement, Cem. Concr. Res. 38 (4) (2008) 543–553, https://doi.org/10.1016/j.cemconres.2007.11.004.

[6] M. Altmaier, V. Blin, D. Garcia, P. Henocq, T. Missana, D. Ricard, J. Vandenborre. State of the Art on Cement-organic-radionuclide Interactions, EURAD Deliverable 3.1 of the HORIZON 2020.

[7] D. Norton, R. Knapp, Transport phenomena in hydrothermal systems: the nature of porosity. Am. J. Sci. 277 (1977) 913–936, https://doi.org/10.2475/ajs.277.8.913.

[8] C.D. Shackelford, S.M. Moore, Fickian diffusion of radionuclides for engineered containment barriers: diffusion coefficients, porosities, and complicating issues, Eng. Geol. 152 (2013) 133–147, https://doi.org/10.1016/j.enggeo.2012.10.014.

[9] H.F.W. Taylor. Cement Chemistry, 1st. Edition, Academic Press, London, 1990. ISBN 0-12-683900-X.

[10] M.I. Khan, R. Siddique, Utilization of silica fume in concrete: review of durability properties, Resour. Conserv. Recycl. 57 (2011) 30–35, https://doi.org/10.1016/j.resconrec.2011.09.016.

[11] E. Özbay, M. Erdemir, H.I. Durmus, Utilization and efficiency of ground granulated blast furnace slag on concrete properties – A review, Constr. Build. Mater. 105 (2016) 423–434, https://doi.org/10.1016/j.conbuildmat.2015.12.153.

[12] R.C. Ewing, Long-term storage of spent nuclear fuel, Nat. Mater. 14 (2015) 252–257, https://doi.org/10.1038/nmat4226.

[13] S.C. Sheppard, L.H. Johnson, B.W. Goodwin, J.C. Tait, D.M. Wuschke, C. C. Davison, Chlorine-36 in nuclear waste disposal – 1. Assessment results for used fuel with comparison to ^{129}I and ^{14}C, Waste Man 16 (1996) 607–614, https://doi.org/10.1016/S0956-053X(97)00001-9.

[14] L.R. Van Loon, M.A. Glaus, W. Muller, Anion exclusion effects in compacted bentonites: towards a better understanding of anion diffusion, Appl. Geochem. 22 (2007) 2536–2552, https://doi.org/10.1016/j.apgeochem.2007.07.008.

[15] C.A.J. Appelo, L.R. Van Loon, P. Wersin, Multicomponent diffusion of a suite of tracers (HTO, Cl, Br, I, Na, Sr, Cs) in a single sample of opalinus clay, Geochim Cosmochim. Acta 74 (2010) 1201–1219, https://doi.org/10.1016/j.gca.2009.11.013.

[16] M.D.A. Thomas, R.D. Hooton, A. Scott, H. Zibara, The effect of supplementary cementitious materials on chloride binding in hardened cement paste, Cem. Concr. Res. 42 (2012) 1–7, https://doi.org/10.1016/j.cemconres.2011.01.001.

[17] A. Ipavec, T. Vuk, R. Gabrovšek, V. Kaučič, Chloride binding into hydrated blended cements: the influence of limestone and alkalinity, Cem. Concr. Res. 48 (2013) 74–85, https://doi.org/10.1016/j.cemconres.2013.02.010.

[18] L. Nedyalkova, J. Tits, E. Bernard, E. Wieland, U. Mäder, Sorption experiments with HTO, 36-Cl, 125-I and 14-C labeled formate on aged cement matrices retrieved from long-term In-situ rock laboratory experiments, J. Adv. Concr. Technol. 19 (2021) 811–829, https://doi.org/10.3151/jact.19.811.

[19] B.F. Greenfield, D.J. Ilett, M. Ito, R. McCrohon, T.G. Heath, C.J. Tweed, S. J. Williams, M. Yui, The Effect of cement additives on radionuclide solubilities, Radiochim Acta 82 (1998) 27–32, https://doi.org/10.1524/ract.1998.82.special-issue.27.

[20] N. Macé, P. Fichet, S. Savoye, J. Radwan, C. Lim, S. Lefèvre, J. Page, P. Henocq, Use of quantitative digital autoradiography technique to investigate the chlorine-36-labelled radiotracer transport in concrete, Appl. Geochem. 100 (2019) 326–334, https://doi.org/10.1016/j.apgeochem.2018.12.014.

[21] C. Grapeloup, S. Cornu, X. Giraud, J. Pupier, A. Team, V. Guillou, P. Ciffroy, B. L. Cabana, C. Couegnas, C. Hatté, L. Benedetti, 36Cl, a new tool to assess soil carbon dynamics, Sci. Rep. 13 (1) (2023) 15085, https://doi.org/10.1038/s41598-023-41555-x.

[22] Gascoyne M. 2014. Chlorine Isotopes and their Application to Groundwater Dating at Olkiluoto.Posiva Working Report 2014-38.

[23] N.S. Sturchio, M. Caffeem, A.D. Beloso, L.J. Heraty, J.K. Böhlke, P.B. Hatzinger, W. A. Jackson, B. Gu, J.M. Heikoop, M. Dale, Chlorine-36 as a tracer of perchlorate origin, Environ. Sci. Technol. 43 (18) (2009) 6934–6938, https://doi.org/10.1021/es9012195.

[24] A. Angileri, P. Sardini, D. Beaufort, G. Amiard, M.F. Beaufort, J. Nicolai, M. Siitari-Kauppi, M. Descostes, Mobility of daughter elements of 238U decay chain during leaching by in situ recovery (ISR): new insights from digital autoradiography, J. Environ. Radioact. 220-221 (2020) 106274, https://doi.org/10.1016/j.jenvrad.2020.106274.

[25] C. Delayre, J. Sammaljärvi, S. Billon, E. Muuri, P. Sardini, M. Siitari-Kauppi, Comparison of phosphor screen autoradiography and micro-pattern gas detector based autoradiography for the porosity of altered rocks, Sci. Rep. 10 (2020) 9455, https://doi.org/10.1038/s41598-020-65791-7.

[26] H. Lefeuvre, J. Donnard, M. Descostes, S. Billon, S. Duval, T. Oger, H. Toubon, P. Sardini, Spectroscopic autoradiography of alpha particles using a parallel ionization multiplier gaseous detector, Nucl. Inst. Methods Phys. Res. A 1035 (2022) 166807, https://doi.org/10.1016/j.nima.2022.166807.

[27] H. Lefeuvre, S. Billon, M. Descostes, J. Donnard, S. Duval, P. Sardini, Using spectroscopic autoradiography of alpha particles for the quantitative mapping of 226Ra ultra-traces in geo-materials, J. Env Rad. 273 (2024) 107392, https://doi.org/10.1016/j.jenvrad.2024.107392.

[28] J.W.L. Ang, A. Bongrand, S. Duval, J. Donnard, J. Parkkonen, S. Utsunomiya, R. Koivula, M. Siitari-Kauppi, G.T.W. Law, Improved radio-cesium detection using quantitative real-time autoradiography, ACS Omega 8 (2023) 22523–22535, https://doi.org/10.1021/acsomega.3c00728.

[29] J.W.L. Ang, A. Bongrand, S. Duval, J. Donnard, E.M. Jolis, S. Utsunomiya, K. Minomo, R. Koivula, M. Siitari-Kauppi, G.T.W. Law, Detecting radioactive particles in complex environmental samples using real-time autoradiography, Sci. Rep. 14 (2024) 5413, https://doi.org/10.1038/s41598-024-52876-w.

[30] F. Li, Kinetic Analysis of Dynamic PET for Molecular, Functional and Physiological Characterization of Diseases (Dissertation), University of Western Ontario, 2020, ⟨https://ir.lib.uwo.ca/etd/7038⟩ (Dissertation).

[31] R. Smith, et al., The α-synuclein PET tracer [18F] ACI-12589 distinguishes multiple system atrophy from other neurodegenerative diseases, Nat. Comm. 14 (2023) 6750, https://doi.org/10.1038/s41467-023-42305-3.

[32] J. Sammaljärvi, L. Jokelainen, J. Ikonen, M. Siitari-Kauppi, Free radical polymerisation of MMA with thermal initiator in brick and grimsel granodiorite, Eng. Geol. 135-136 (2012) 52–59, https://doi.org/10.1016/j.enggeo.2012.03.005.

[33] J. Sammaljärvi, M. Shroff Rama, J. Ikonen, E. Muuri, K.-H. Hellmuth, M. Siitari-Kauppi, Free radical polymerisation of methacrylates with thermal initiator in clay rock, Eng. Geol. 210 (2016) 70–83, https://doi.org/10.1016/j.enggeo.2016.06.003.

[34] S. Gaboreau, D. Pret, E. Tinseau, F. Claret, D. Pellegrini, D. Stammose, 15 years of in situ cement-argillite interaction from tournemire URL: characterisation of the multi-scale spatial heterogeneities of pore space evolution, Appl. Geochem. 26 (2011) 2159–2171, https://doi.org/10.1016/j.apgeochem.2011.07.013.

[35] S. Gaboreau, C. Lerouge, S. Dewonck, Y. Linard, X. Bourbon, C.I. Fialips, A. Mazurier, D. Pret, D. Borschneck, V. Montouillout, E.C. Gaucher, F. Claret, In-Situ interaction of cement paste and shotcrete with claystones in a deep disposal context, Am. J. Sci. 312 (2012) 314–356, https://doi.org/10.2475/03.2012.03.

[36] J. Jeong, P. Sardini, H. Ramezani, M. Siitari-Kauppi, H. Steeb, Modeling of the induced chemo-mechanical stress through porous cement concrete subjected to CO2: enhanced micro-dilatation theory and 14C-PMMA method, Comput. Mater. Sci. 69 (2013) 466–480, https://doi.org/10.1016/j.commatsci.2012.11.031.

[37] J.C. Robinet, P. Sardini, M. Siitari-Kauppi, D. Prêt, B. Yven, Upscaling the porosity of the callovo-oxfordian mudstone from the pore scale to the formation scale; insights from the 3H-PMMA autoradiography technique and SEM BSE imaging, Sediment. Geol. 321 (2015) 1–10, https://doi.org/10.1016/j.sedgeo.2015.02.007.

[38] P. Lalan, A. Dauzères, L. DeWindt, D. Bartier, J. Sammaljärvi, J.-D. Barnichon, I. Techer, V. Detilleux, Impact of a 70 °C temperature on an ordinary portland cement paste/ claystone interface: an in situ experiment, Cem. Concr. Res. 83 (2016) 164–178, https://doi.org/10.1016/j.cemconres.2016.02.001.

[39] P. Lalan, A. Dauzères, L. De Windt, J. Sammaljärvi, D. Bartier, I. Techer, V. Detilleux, M. Siitari-Kauppi, Mineralogical and microstructural evolution of portland cement paste/argillite interfaces at 70 °C – Considerations for diffusion and porosity properties, Cem. Concr. Res. 115 (2019) 414–425, https://doi.org/10.1016/j.cemconres.2018.09.018.

[40] A. Möri, et al, 2003. The Nagra-JNC in situ study of Safety Relevant Radionuclide Retardation in Fractured Crystalline Rock. IV: the in Situ Study of Matrix Porosity in the Vicinity of A Water Conducting Fracture. Technical Report. 00–08. Nagra, Wettingen/ Switzerland.

[41] A. Blumstein, Polymerization of adsorbed monolayers. I. Preparation of clay-polymer complex, J. Pol. Sci. Part A 3 (1965) 2653–2664.

[42] P. Sardini, L. Caner, P. Mossler, A. Mazurier, K.H. Hellmuth, R. Graham, A. Rossi, M. Siitari-Kauppi, Calibration of digital autoradiograph technique for quantifying rock porosity using ^{14}CPMMA method, J. Radioanal. Nucl. Chem. 303 (1) (2015) 11–23, https://doi.org/10.1007/s10967-014-3617-9.

[43] J. Donnard, R. Berny, H. Carduner, P. Leray, E. Morteau, M. Provence, N. Servagent, D. Thers, The micro-pattern gas detector PIM: a multi-modality solution for novel investigations in functional imaging, Nucl. Instrum. Methods Phys. Res A 610 (1) (2009) 158–160, https://doi.org/10.1016/j.nima.2009.05.186.

[44] L'Annunziata (ed). 2003. Handbook of Radioactivity Analysis. 2nd edition. Pages 1063-1127. ISBN: 9780080495057.

[45] S. Billon, P. Sardini, S. Leblond, P. Fische, From Bq cm−3 to Bq cm−2 (and conversely)—part 1: a useful conversion for autoradiography, . 2019, J. Radioanal. Nucl. Chem. 320 (2019) 643–654, https://doi.org/10.1007/s10967-019-06521.

[46] C.A.J. Appelo, D. Postma. Geochemistry, Groundwater and Pollution, 2nd ed., CRC Press, 2005, pp. 75–95, https://doi.org/10.1201/9781439833544.

[47] C.A.J. Appelo, Solute transport solved with the Nernst-Planck equation for concrete pores with 'free' water and a double layer, Cem. Conc. Res 101 (2017) 102–113, https://doi.org/10.1016/j.cemconres.2017.08.030.

[48] F.R. de Hoog, J.H. Knight, A.N. Stokes, An improved method for numerical inversion of laplace transforms, SIAM J. Sci. Stat. Comput. 3 (1982) 357–366, https://doi.org/10.1137/0903022.

[49] S.S. Augustithis (Ed.), Leaching and Diffusion in Rocks and their Weathering Products, Theophrastus Publications, Athens, Greece, 1983, p. 6.

[50] J.H. Wang, Self-diffusion coefficients of water, J. Phys. Chem. 69 (12) (1965) 4412, https://doi.org/10.1021/j100782a510.

[51] B. Zehtab, A. Tarighat, Diffusion study for chloride ions and water molecules in C-S-H gel in nano-scale using molecular dynamics: case study of tobermorite, Adv. Concr. Constr. 4 (4) (2016) 305–317, https://doi.org/10.12989/acc.2016.4.4.305.

[52] E. Samson, J.- Marchand, K.A. Snyder, Calculation of ionic diffusion coefficients on the basis of migration test results, . 2003, Mater. Struct. 36 (2003) 156–165, https://doi.org/10.1007/BF02479554.
[53] ACI, Guide for the Use of Silica Fume in Concrete. ACI Committee Report ACI 234R-96, American Concrete Institute, 1996.
[54] K.-H. Hellmuth, J. Sammaljärvi, M. Siitari-Kauppi, J.-C. Robinet, P. Sardini, STED nanoscopy – a novel way to image the pore space of geological materials, J. Microsc. 283 (2021) 151–165, https://doi.org/10.1111/jmi.13016.
[55] A. Tabarelli, E. Oliari Garcez, F. Machado Nunes, C. Monteiro Cholant, S. Brand Scheibler, C. Oropesa Avellaneda, Investigating the effect of curing in the chloride diffusion coefficient of conventional concrete, Mater. Res. 22 (. 1) (2019) e20190160, https://doi.org/10.1590/1980-5373-MR-2019-0160.
[56] H. Jin, Z. Li, W. Zhang, J. Liu, R. Xie, L. Tang, J. Zhu, Iodide and chloride ions diffusivity, pore characterization and microstructures of concrete incorporating ground granulated blast furnace slag, J. Mat. Res. Technol. 16 (2022) 302–321, https://doi.org/10.1016/j.jmrt.2021.11.155.
[57] K. Uusheimo, A. Muurinen, J. Lehikoinen and M. Olin. Diffusion in Concrete, Crushed Rock and Mixtures of Crushed Rock and Bentonite. 1993. Technical Report YJT-93-26. Finland.
[58] S. Caré, Influence of aggregates on chloride diffusion coefficient into mortar, Cem. Concr. Res. 33 (2003) 2021, https://doi.org/10.1016/S0008-8846(03)00009-7, 1028.